

Coma composition of comet 67P/Churyumov-Gerasimenko from radio-wave spectroscopy*,**,***

N. Biver¹, D. Bockelée-Morvan¹, J. Crovisier¹, Aa. Sandqvist², J. Boissier³, D. C. Lis⁴, M. Cordiner^{5,6}, B. P. Bonev⁷, N. Dello Russo⁸, R. Moreno¹, S. Milam⁵, N. X. Roth^{5,6}, R. Vervack⁸, and M. A. DiSanti⁹

- ¹ LESIA, Observatoire de Paris, PSL Research University, CNRS, Sorbonne Université, Université Paris-Cité, 5 place Jules Janssen, 92195 Meudon, France
 - e-mail: nicolas.biver@obspm.fr
- ² Stockholm Observatory, Stockholm University, SCFAB-AlbaNova, 10691 Stockholm, Sweden
- ³ IRAM, 300 rue de la Piscine, 38406 Saint-Martin-d'Hères, France
- ⁴ Jet Propulsion Laboratory, California Institute of Technology, 4800 Oak Grove Drive, Pasadena, CA 91109, USA
- ⁵ Solar System Exploration Division, Astrochemistry Laboratory Code 691, NASA-GSFC, Greenbelt, MD 20771, USA
- Department of Physics, Catholic University of America, Washington, DC 20064, USA
- Department of Physics, American University, 3501 Nebraska Ave NW, Washington, DC 20016, USA
- ⁸ Johns Hopkins University Applied Physics Laboratory, 11100 Johns Hopkins Rd., Laurel, MD 20723, USA
- ⁹ Solar System Exploration Division, Planetary System Laboratory Code 693, NASA-GSFC, Greenbelt, MD 20771, USA

Received 12 December 2022 / Accepted 24 February 2023

ABSTRACT

We present the results of a molecular survey of comet 67P/Churyumov-Gerasimenko undertaken with the Institut de RadioAstronomie Millimétrique (IRAM) 30-m radio telescope in November-December 2021, when it had its most favourable apparition in decades. Observations at IRAM 30-m during the 12-16 November period covered 8 GHz bandwidth at 3 mm, 16 GHz at 2 mm, and 60 GHz in the 1 mm window domain. These were completed by snapshots at 1 mm on 12-13 December and a short observation of the H₂O line at 557 GHz with the Odin sub-millimetre observatory on 17.0 November 2021, and with 18-cm observations of OH with the Nançay radio telescope. Less sensitive observations obtained at a previous perihelion passage on 18-22 September 2015 with IRAM and 9-12 November 2015 with Odin are also presented. The gas outflow velocity, outgassing pattern, and temperature have been accurately constrained by the observations. They are perfectly consistent with those measured in situ with the Rosetta/MIRO sub-millimetre instrument in 2015. In particular, the asymmetry of the line is well represented by a jet concentrating three-quarters of the outgassing in about π steradians. We derived abundances relative to water for seven molecules and significant upper limits for approximately five others. The retrieved abundances were compared to those measured in situ at the previous perihelion with Rosetta. While those of HCN, CH₃OH, and HNCO are comparable, 67P is found to be depleted in H₂S and relatively normal in CS (H₂S/CS \approx 3) in strong contradiction with the Rosetta/ROSINA mass spectrometer measurement of the H₂S/CS₂ (≈100) abundance ratio. While the formaldehyde total abundance found with IRAM 30-m when assuming it to be mostly produced by a distributed source (Haser parent scale length ≈8000 km) is similar to the one derived by Rosetta/ROSINA, we find that the formaldehyde coming from the nucleus is one order of magnitude less abundant than measured in situ by Rosetta/ROSINA.

Key words. comets: general – comets: individual: 67P/Churyumov-Gerasimenko – radio lines: planetary systems – submillimeter: planetary systems

1. Introduction

Comets are the most pristine remnants left over from the formation of the Solar System 4.6 billion years ago. They contain a sample of the oldest and most primitive material in the Solar

System, including ices, rendering them our best window on the volatile composition of the solar proto-planetary disk. Formed beyond the ice line in the outer part of the Solar System, they have remained outside the orbit of Pluto for most of their lifetime, either in the Oort cloud or in the trans-Neptunian scattered disk (within the Kuiper belt). This latter reservoir is supplying the ecliptic short-period comets (also called Jupiter-family comets), which have been the targets of several space missions due to their more easily accessible trajectories.

Comet 67P/Churyumov-Gerasimenko is a Jupiter-family comet (JFC) orbiting the Sun in 6.4 yr on a low inclination (3.9°) orbit. It was extensively investigated by the ESA Rosetta mission in 2014–2016 (Accomazzo et al. 2016, 2017) around its perihelion passage, which occurred on 13.1 August 2015 UT at a heliocentric distance of $r_h = 1.243$ au. Its next perihelion took place on 2.1 November 2021 UT at $r_h = 1.211$ au. This apparition was much more favourable than the previous one for Earth-based

^{*} The radio spectra are only available at the CDS via anonymous ftp to cdsarc.cds.unistra.fr (130.79.128.5) or via https://cdsarc.cds.unistra.fr/viz-bin/cat/J/A+A/672/A170

^{**} Based on observations carried out with the IRAM 30-m telescope. IRAM is supported by INSU/CNRS (France), MPG (Germany), and IGN (Spain).

^{***} Odin is a Swedish-led satellite project funded jointly by the Swedish National Space Board (SNSB), the Canadian Space Agency (CSA), the National Technology Agency of Finland (Tekes), the Centre National d'Études Spatiales (CNES, France), and the European Space Agency (ESA). The Swedish Space Corporation, today OHB Sweden, is the prime contractor, also responsible for Odin operations.



Fig. 1. Optical image of the comet 67P taken just before the beginning of the IRAM observations on 11.198 November 2021. This is a 3.6 min exposure obtained with a 40.7-cm telescope at F/D = 4.3 from Eure-et-Loire (France). North is up. Left panel: Colour image with a field of view of $40 \times 40'$, showing greenish C_2 coma, dust coma with asymmetry to the lower left and dust tail. Right panel: Grey-scale image after applying a 15° rotational gradient to emphasise the sunward jet to the lower left and dust tail. As in Fig. 2, the inset shows the pole orientation and illumination (in blue) of the nucleus at the time of the observations. The jet orientation (position angle, $PA \sim 120^{\circ}$) is intermediate between the sun direction ($PA = 99^{\circ}$) and the south pole direction ($PA = 154^{\circ}$).

observations, as it approached Earth four times closer, at 0.42 au on 12 November 2021. It was also its second closest approach to Earth after the one of 1982 and its closest perihelion in at least three centuries. Figure 1 shows the comet at the 2021 perigee showing the typical sunward jet feature (enhanced in the left panel) present during its whole apparition. The geometry of the orientation of the rotation axis based on its 2015 apparition and the illumination of the nucleus is illustrated in the lower right corner of the figure.

We observed comet 67P with the Institut de RadioAstronomie Millimétrique (IRAM) 30-m telescope between 12.0 and 16.4 November and on 12.4 and 13.4 December 2021 UT. In parallel, the Odin sub-millimetre space observatory aimed to detect and map the emission of H₂O at 557 GHz, but the observations partly failed due to tracking issues. The comet was also observed in 2015 with IRAM 30-m (18.3–22.4 September 2015) and Odin (9.5–12.1 November 2015), but with much lower sensitivity. The results reported earlier in Snodgrass et al. (2017) are detailed here.

In this paper, we report the detection of H_2O , HCN, CH_3CN , CH_3OH , H_2CO , H_2S , CS, HNCO, and significant upper limits for half a dozen additional molecules. Section 2 presents the observations and spectra of the detected molecules. The information extracted from the observations to analyse the data and compute production rates is provided in Sect. 3. In Sect. 4, we present the retrieved production rates and abundances or upper limits, which are discussed and compared to in situ observations in Sect. 5.

2. Observations of comet 67P

Comet 67P/Churyumov-Gerasimenko was the subject of an intense worldwide observing campaign in 2014–2016 in

conjunction with the in situ exploration by the Rosetta spacecraft. Global results have been reported in Snodgrass et al. (2017). We contributed via the millimetre to sub-millimetre spectroscopic investigations with the IRAM 30-m and Odin sub-millimetre satellite. At its favourable 2021 perihelion return, comet 67P was also the focus of an observing campaign and we contributed via observations conducted with the same facilities. The log of these observations is reported in Tables A.1 and A.2.

2.1. Observations with the IRAM 30-m

In September 2015, comet 67P/Churyumov-Gerasimenko was the focus of the IRAM 30-m proposal 001-15. Observations were taking place during the daytime between 18 and 22 September. Weather conditions were generally not optimal, degrading in the middle of the day, with the sky getting cloudy and unstable, and showing an increasing opacity with more than 7 mm of precipitable water vapour (*pwv*). Weather conditions were bad all day on 21 September, and the best data were obtained during three mornings: 18.2–18.4, 20.2–20.4 and 21.2–21.4 September UT, when *pwv* was below 4 mm (Table A.1).

Comet 67P/Churyumov-Gerasimenko was the target of the observing proposal 001-21 scheduled at the IRAM 30-m telescope between 12 and 16 November 2021. Weather conditions were average to very good, with *pwv* in the 1.2–6.5 mm range (Table A.2). The best observing conditions were met on the last two nights. Two other snapshots (less than 1/2 h of observations) were obtained on 12 and 13 December at the beginning of observing run 100-21 when the other comet target was not yet available.

We used the EMIR (Eight MIxer Receiver, Carter et al. 2012) 3 mm, 2 mm, and 1 mm band receivers in 2SB mode connected to the FTS (Fast Fourier Transform Spectrometer) and the

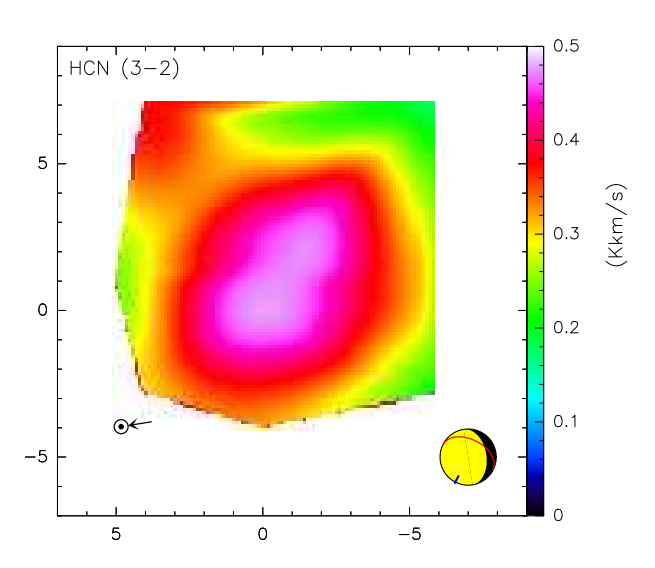


Fig. 2. Coarse map of the HCN(3–2) line-integrated intensity on 16.11 November 2021. We note that X and Y scales are in arcsec relative to the location of the peak of intensity (colour scale on the right). The graphic in the lower right indicates the orientation of the rotation axis (Earth sub-latitude is -41°) and solar illumination (phase 48.6° , direction PA = 98.6° , indicated also in the lower left).

VESPA (VErsatile SPectrometer Array) high-resolution spectrometer (see Tables A.1 and A.2). Observations were obtained in wobbler switching mode with the secondary (wobbling) mirror alternating pointing between the ON and OFF positions separated by 180" every 2 s. In 2015, a few observations were carried out using the Frequency SWitching mode (FSW), with a throw of 7.4–7.8 MHz, as we were targeting only a few strong lines (Table A.1) and not aiming at a frequency survey. The wobbler failed on 14.0 November 2021 and we had to change to the position switch mode (PSW) for the next two and a half shifts until it could be repaired. The reference OFF positions in PSW mode were at 300", alternating ON and OFF every 15 s.

Comet 67P was tracked using the latest JPL Horizons¹ orbital elements available: #K084/23 in 2015 and #K212/16 in 2021. In 2021, offsets between positions computed by the telescope control software and those of the Horizons tool were taken into account because of the proximity of the comet. Residual offsets between the latest astrometric measurements and the JPL Horizons ephemerides were small (<0.5") and coarse maps of HCN were used to estimate residual offsets, generally below 1" in RA or Dec (Fig. 2).

IRC+10216 and ORION molecular clouds were used as line intensity reference sources and Uranus and Mars were used to check the main beam efficiency. Corrections had to be applied to the V polarisation at high frequencies (250–270 GHz) to compensate for the $\sim\!20\%$ loss in line intensities due to impurity of the local oscillator signal. In 2015, we also used IRC+10216 and Mars as reference calibration sources.

2.2. Observations with Odin

Observations with the Odin sub-millimetre observatory (Frisk et al. 2003) were planned during 40 orbits (corresponding to about 1h ON+OFF source for each) between 9.47 and 12.10 November 2015 UT and 13 orbits from 16.70 to 17.54 November 2021 UT. In 2015, observations could not take place earlier due to elongation constraints that prevent observations with Odin closer

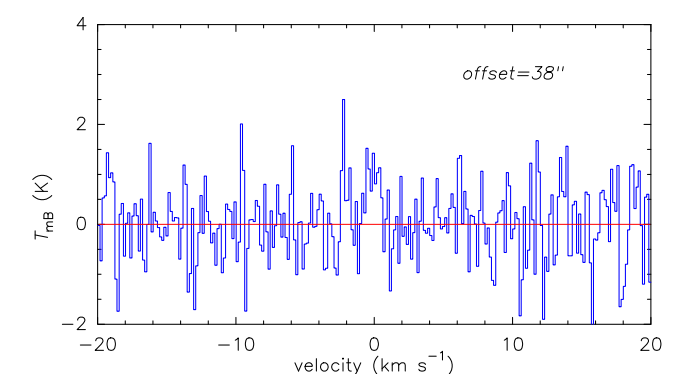


Fig. 3. $H_2O(1_{10}-1_{01})$ line at 556935.988 MHz observed with Odin in comet 67P on 17.00 November 2021. The vertical axis is the main beam brightness temperature in kelvins, and the horizontal axis is the Doppler velocity in the rest frame of the comet with respect to the line. The average pointing offset during the 2 min drift of the comet through the beam is 38".

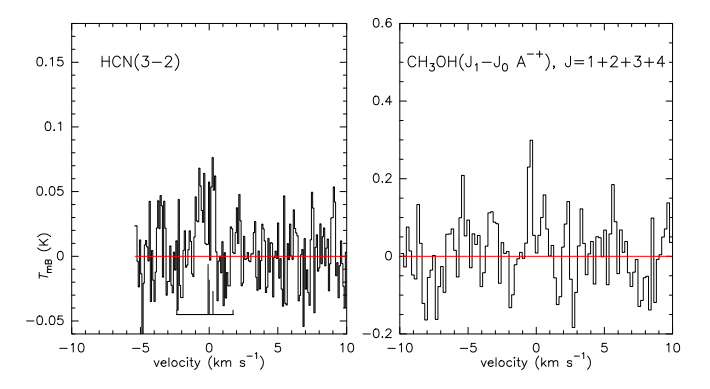


Fig. 4. Millimetre lines observed with IRAM 30-m in comet 67P in 2015. Left panel: HCN(3–2) line at 265886.434 MHz with the position and relative intensity of the hyperfine component shown from the average of 18.25 to 20.40 September 2015. Right panel: Sum of the four CH₃OH lines at 303366.893, 304208.324, 305473.472, and 307165.911 MHz observed on 22.30 September 2015. The vertical axis is the main beam brightness temperature in kelvins, and the horizontal axis is the Doppler velocity in the rest frame of the comet with respect to the main line.

than 60° from the Sun. In 2021, unfortunately, likely due to a programming error, the comet was tracked at ~10 times its real motion on the sky and was within the telescope beam for only 2 min around 17.000 November UT. The same setup was used in both cases, with two receivers 549A1 and 555B2 tuned at the frequency of the $H_2O(1_{10}-1_{01})$ line at 556935.988 MHz, with AutoCorrelatorS (ACS) connected to each of them, providing a ~0.08 km s⁻¹ spectral resolution. The 1 GHz bandwidth and 1 MHz resolution acousto optical spectrometer (AOS) was connected to the 555B2 receiver. The line was not detected in 2015 and the ACS average water spectrum of 2021 is shown in Fig. 3.

2.3. Spectra and line intensities

The best 2015 spectra, the 3-day integration on HCN(3–2), and the sum of the four strongest CH₃OH lines at 301–307 GHz on 22.3 September are shown in Fig. 4. A selection of the strongest lines observed with IRAM 30-m, with averages over the 12–16 November 2021 period, is shown in Figs. 5–6. The line intensities are provided in Tables A.3 and A.4, with averages over several days when the signal-to-noise ratio (S/N) was too low in a single observation.

https://ssd.jpl.nasa.gov/horizons.cgi

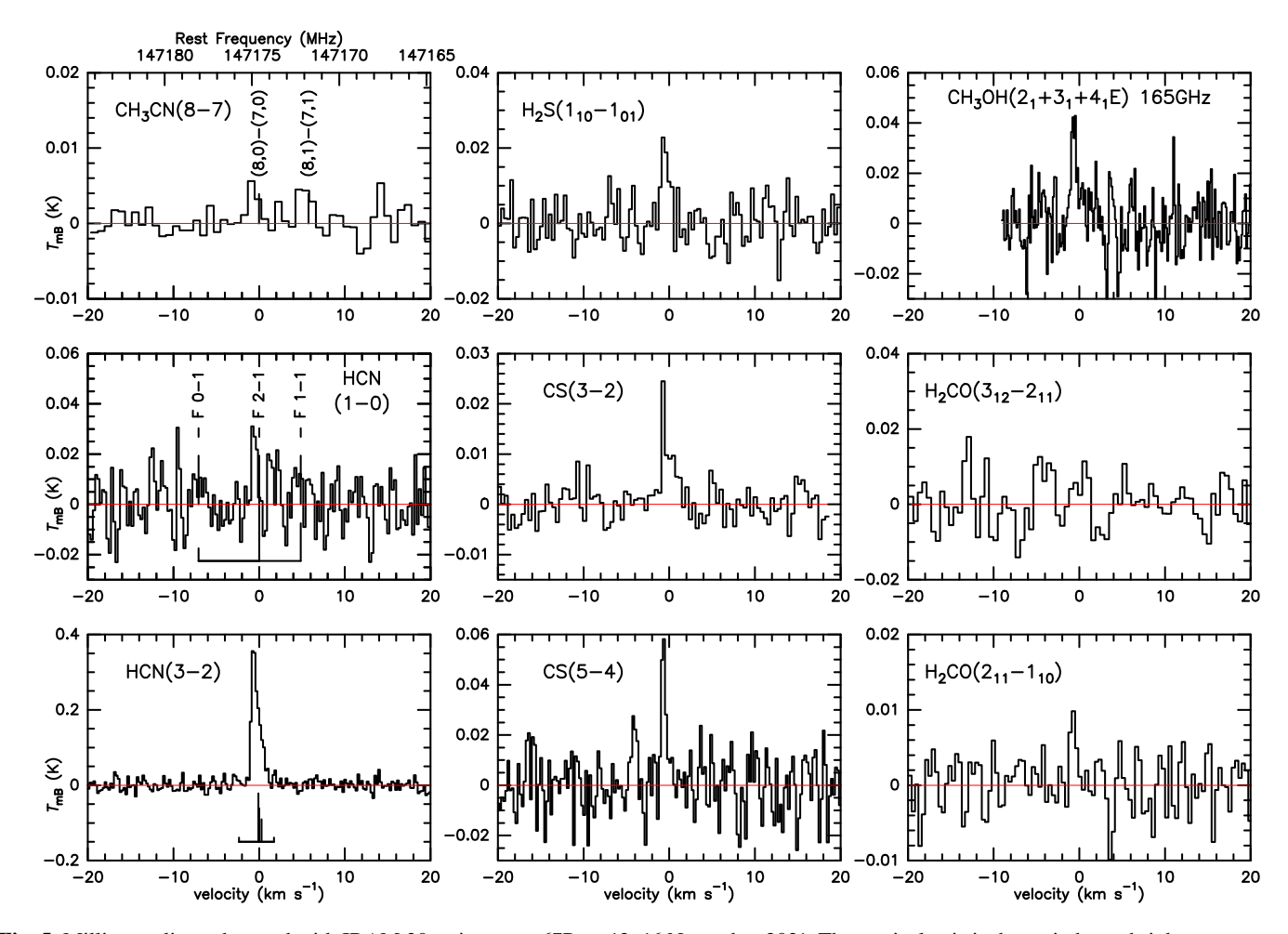


Fig. 5. Millimetre lines observed with IRAM 30-m in comet 67P on 12–16 November 2021. The vertical axis is the main beam brightness temperature in kelvins, and the horizontal axis is the Doppler velocity in the rest frame of the comet with respect to the main line. For methanol, we have chosen to show, at high spectral resolution, the sum of the three strongest lines observed around 165 GHz with the VESPA correlator.

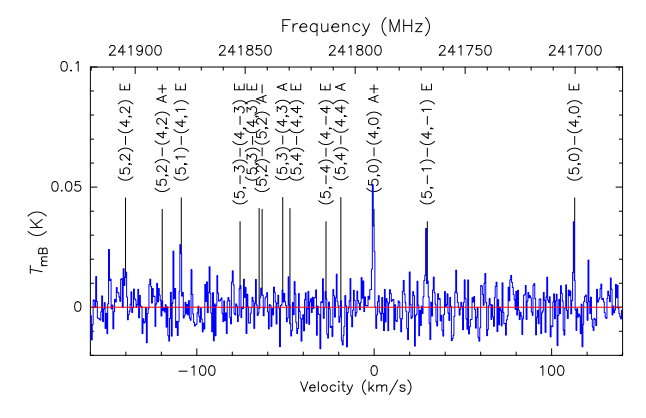


Fig. 6. CH₃OH lines around 242 GHz observed with IRAM 30-m in comet 67P on 12.2–16.1 November 2021. The vertical axis is the main beam brightness temperature in kelvins, and the horizontal axis is the Doppler velocity in the rest frame of the comet (reference line is the $5_0 - 4_0A$ at 241791.367 MHz) with rest frequency scale on the upper axis.

2.4. Observations with the Nançay radio telescope: OH 18-cm lines

Comet 67P/Churyumov-Gerasimenko was not observed at Nançay during its 2015 passage because of its unfavourable geocentric distance. For the much more favourable 2021 passage,

observations were scheduled from 12 September 2021 to 31 January 2022. The telescope characteristics, observing procedure, and data analysis are as described by Crovisier et al. (2002), except that in September-October, the daily observations were limited to about 30 min instead of 1 h due to work on the focal track. Unfortunately, 67P could not be observed simultaneously with the IRAM observations because the expected OH inversion was too low to guarantee a detection at that time (inversion was typically lower than 0.10 in absolute value).

We focus here on two average spectra, those from 26 September to 25 October and those from 20 December 2021 to 1 January 2022. The spectra used here for the analysis are averages of the 1667 and 1665 MHz lines converted to the 1667 intensity scale. They are shown in Fig. 7 and their parameters are listed in Table 1. It can be noted that the OH line in October showed a blueshift similar to that observed for parent molecules at IRAM, which can be explained by the asymmetric outgassing.

3. Data analysis

3.1. Expansion velocity and outgassing pattern

All lines display a strong asymmetry with a mean blueshift around -0.3 km s^{-1} (Tables A.3 and A.4), indicative of a very asymmetric outgassing with the majority of the gas being ejected in the direction of the observer. Fitting two Gaussians to the lines

Table 1. Parameters of the OH 18-cm lines observed with the Nançay radio telescope and production rates in 2021.

UT date	$\langle \Delta \rangle$	$\langle r_{ m h} angle$	$\dot{r}_{ m h}$	inv ^(a)	inv ^(b)	$T_{ m bg}$	Line area	Doppler shift	Prod. rate ^(a)
(mm/dd.dd-dd.dd)	(au)	(au)	$(km s^{-1})$			(K)	$(mJy km s^{-1})$	$(km s^{-1})$	(molec s ⁻¹)
09/26.17–10/25.11 12/20.12–12/32.09	0.47 0.47	1.25 1.38	-5.0 +10.0	-0.23 -0.16	-0.28 -0.18	3.4 3.1	-51 ± 6 -43 ± 6	**** = ****	$1.1 \pm 0.1 \times 10^{28}$ $2.0 \pm 0.3 \times 10^{28}$

Notes. ^(a)Maser inversion and OH production rate using the Despois et al. (1981) inversion model and a OH lifetime of 0.95×10^5 s at 1 au. ^(b)Maser inversion model from Schleicher & A'Hearn (1988); the corresponding Q_{OH} would be 0.9 and 1.8×10^{28} molec s⁻¹, respectively.

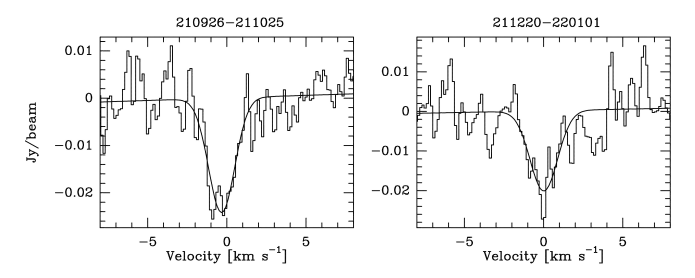


Fig. 7. Averaged OH 18-cm lines observed with the Nançay radio telescope. The vertical axis is the flux in janskys, and the horizontal axis is the Doppler velocity in the rest frame of the comet.

with the best S/N yields, on average, velocities at half maximum intensity (VHM) of -0.95 ± 0.03 and $+0.55 \pm 0.08$ km s⁻¹ in 2021. Taking into account the broadening due to the hyperfine structure of HCN and thermal broadening, in order to fit the asymmetry of the line, expansion velocities of 0.86 km s⁻¹ on the observer side and 0.54 km s⁻¹ on the opposite side are necessary.

In order to fit both the line width and mean blueshift, we modelled the outgassing with a two-component pattern: a jet at 0.86 km s⁻¹ in a solid angle $\Omega_j = \pi$ sr oriented towards the Sun and observer and the remaining $4\pi - \Omega_j$ sr component expanding at 0.54 km s⁻¹. The fraction of total outgassing in the jet was adjusted so that the simulated line blueshifts would be close to the observed value.

To simulate the HCN line profile (Fig. 8, which also shows the geometry of outgassing), the π sr jet is a half hemisphere defined by its angular domain in spherical coordinates (colatitude defined from the z-axis $\phi = 0-90^{\circ}$ and azimuth range $\theta = \pm 90^{\circ}$), with the z-axis in the direction of the observer. As such, this jet can cover the direction of the observer and the direction of the Sun (phase angle $\phi \approx 48^{\circ}$) and the south pole (at 49° from the observer direction). The Sun and south pole directions are not in the same projected direction in the plane of the sky (position angle, $PA = 99^{\circ}$ and 154°) but they are covered by the width (180° along the θ angle which is similar to PA but with an as of yet unspecified or different origin). The optical counterpart (Fig. 1) of the jet seems to be at an intermediate position (PA $\sim 120^{\circ}$). Radio observations centred on the nucleus are not sensitive to the orientation of the jet in the plane of the sky and do not define an origin of θ (the asymmetry seen in Fig. 2 is unlikely significant as the map only covers one beam size of 9.3"). Assuming dust in the optical image follows the gas, we can assume that the gas jet is roughly centred around PA = 120° to define the reference $\theta = 0$. We do not have a very strong constraint on the opening of the jet component. But a wider jet $(1-2 \pi \text{ sr})$ would require the jet to be more directed towards the observer than the Sun or pole in order to fit the shape and Doppler shift.

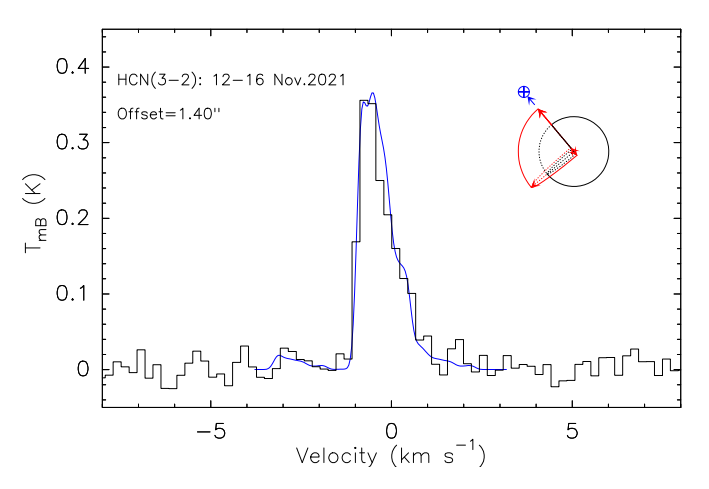


Fig. 8. HCN(3–2) line profile (average of 12.1 to 16.2 November 2021) with a simulation superimposed in blue. The vertical axis is the main beam brightness temperature in kelvins, and the horizontal axis is the Doppler velocity in the rest frame of the comet. The inset to the upper right depicts the outgassing pattern used to model the line: $Q_{\rm HCN} = 0.9 \times 10^{25}$ molec s⁻¹ in a π sr (half of the hemisphere on the Earth side) jet at 0.86 km s⁻¹ and $Q_{\rm HCN} = 0.2 \times 10^{25}$ molec s⁻¹ at 0.54 km s⁻¹ in the remaining 3π sr.

To obtain the right mean Doppler shift of the lines, we adjusted the fraction of the total production inside the jet. To obtain the simulation in Fig. 8, we assumed that 82% (0.9 \times 10^25 of the 1.1 \times 10²⁵ molec s⁻¹ of HCN produced) of the outgassing is in the jet. The simulated mean Doppler shift is $-0.36~\rm km~s^{-1}$ for most lines. We used this outgassing pattern model: 82% in a π sr jet at $v_{\rm exp}=0.86~\rm km~s^{-1}$ and 18% in the remaining 3π sr at 0.54 km s⁻¹. The gas temperature was kept the same in both components.

This approximate modelling to fit the line shapes matches the outgassing pattern observed in situ by the MIRO instrument of Rosetta in 2015 relatively well: a jet centred between the south pole and sub-solar point, with a full width at half maximum of ~120°, corresponding to 1.2π sr and a peak velocity of 0.88 km s⁻¹, for the perihelion time in 2015 (Biver et al. 2019).

A similar model was used for the 2015 IRAM data, but the low S/N of the line shapes cannot provide stringent constraints (VHM = -0.72 ± 0.07 and VHM = $+0.54 \pm 0.08$ from the average of the two lines in Fig. 4).

Assuming isotropic outgassing with a mean expansion velocity of 0.75 km s⁻¹ (0.7 km s⁻¹ in 2015) would give similar results in terms of relative production rates: the asymmetric jet model used yields production rates larger by $5 \pm 2\%$ for all species except for water observed with Odin in 2021. Due to the increased opacity of the $H_2O(1_{10}-1_{01})$ line in the jet, the derived water production rate was increased by 20%.

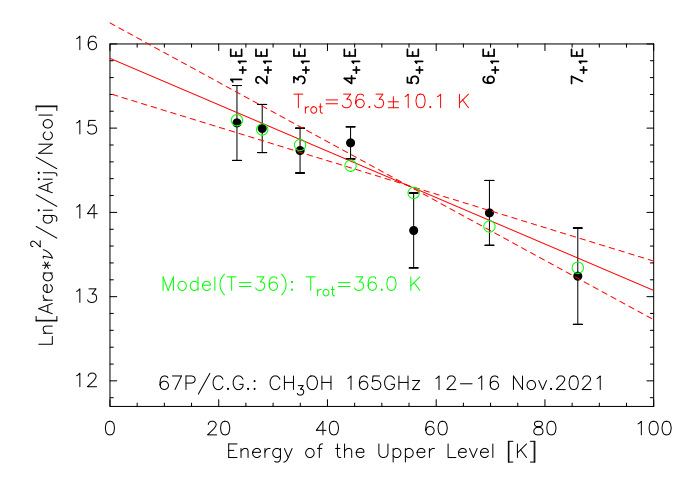


Fig. 9. Rotational diagram of the 12–16 November average of the methanol lines around 166 GHz in comet 67P. The neperian logarithm of a quantity proportional to the line intensity is plotted against the energy of the upper level of each transition. The fit is shown with a solid red line and errors are displayed with red dashed lines. The black dots are the measurements and green circles are the predicted values for a model with a gas temperature of 36 K.

3.2. Gas temperature

The rotational temperatures of two series of methanol lines measured in 2021 are T_{rot} (166 GHz, seven lines) = 36 ± 10 K (Fig. 9) and T_{rot} (242 GHz, seven lines) = 24 ± 5 K. The first series is expected to provide a direct measurement of the gas temperature T, while, in the second case, a gas temperature of T = 36 K implies a lower rotational temperature of $T_{\text{rot,mod}}$ (242 GHz, 7 lines) = 24 and 25.6 K for the isotropic and jet outgassing patterns, respectively, due to faster relaxing towards cold fluorescence equilibrium of the population of the corresponding energy levels (Bockelée-Morvan et al. 1994), which is fully compatible with the measurements. We adopted the value T = 36 K, which is comparable to the 'final' (beyond a few hundreds of kilometres from the nucleus) values measured in situ with MIRO $(T_f = 40 \pm 9 \text{ K and } T(\Delta) = 34 \pm 11 \text{ K, for the August-October}$ 2015 period, Table A.2, Biver et al. 2019). In 2015, we assumed T = 30 K, since the comet was further away from IRAM 30-m than in 2021, thus sampling cooler regions of the coma.

3.3. Reference water production rate

We used the water production rate derived from the observation of the ${\rm H_2^{16}O}$ line with Odin, $Q_{\rm H_2O}=1.2\times10^{28}$ molec ${\rm s^{-1}}$. This value is larger than the peak value estimated in 2015 with MIRO $(0.8\times10^{28}~{\rm molec~s^{-1}},~{\rm Biver~et~al.~2019})$, but lower than the ROSINA reference peak value in 2015 $(1.85\times10^{28}~{\rm molec~s^{-1}},~{\rm Läuter~et~al.~2020})$, obtained by a very different technique and analysis. Higher production rates in 2021 could be expected as the perihelion distance was closer (by 3%) and the comet was displaying a steep heliocentric variation of its water production rate in 2015 $(\propto r_{\rm h}^{-6.5} - r_{\rm h}^{-5.0})$, implying an extrapolated 20% increase in 2021.

The water production rate inferred from the Nançay 26 September to 25 October average is $1.2 \pm 0.1 \times 10^{28}$ molec s⁻¹, which is comparable to that obtained by Odin on 17.0 November. The production rate at the end of December increased by a factor of two. A similar increase was observed at IRAM for CH₃OH between mid-November and mid-December, whereas HCN was steady. The OH maser inversion from Schleicher & A'Hearn

Table 2. Production rates in 67P in September–November 2015.

UT date (mm/dd.dd)	Molecule	r _h (au)	Production rate (×10 ²⁵ molec s ⁻¹)	Lines (a)
11/09.5–12.1	H_2O	1.634	<330	(1)
09/18.3–20.4	HCN	1.324	0.89 ± 0.18	1
09/22.3	CH_3CN	1.337	<2.5	(4)
09/18.4-20.6	CS	1.325	< 2.0	(2)
09/22.3	H_2S	1.337	<16.0	(1)
09/18.4-22.4	CH_3OH	1.330	17 ± 5	(9)
09/18.4-20.6	H_2CO	1.325	<6.3	(3)
	H_2CO_d		<12.2 ^(b)	(3)

Notes. ^(a)Number of lines used for the determination of Q, which are in parentheses when individual lines are not clearly detected. ^(b)Where we assume that H_2CO is produced in the coma by a distributed (H_2CO_d) source and follows a Haser daughter species density profile with a parent-scale length of 8500 km.

(1988, Col. 6 of Table 1) predicts a \approx 10% stronger absorption than from the Despois et al. (1981) model used (Col. 5). This would decrease the water production rate derived from Nançay data in October and in December, bringing them closer to the other measurements from Odin and in the infrared.

Preliminary water production from comet 67P has also been estimated from infrared observations of water hot-bands: 0.8×10^{28} molec s⁻¹ (14 October), 1.1×10^{28} molec s⁻¹ (1–2 November), 1.9×10^{28} molec s⁻¹ (28 November), and 1.5×10^{28} molec s⁻¹ (16 December) (Bonev et al. 2022; Gibb et al. 2022, and priv. comm.).

4. Production rates and abundances

We computed the production rates using both the isotropic and asymmetric jet outgassing patterns, using non-LTE (local thermal equilibrium) excitation codes (Biver et al. 2021a). We provide values in Tables 2 and 3 based on the jet model as described in Sect. 3.1 for all observed molecules, including upper limits. We also provide daily values for molecules detected with a sufficient S/N. As stated in Sect. 3, production rates derived with the isotropic model would only be 3–7% lower. We used the same model for the Odin $H_2O(1_{10}-1_{01})$ line, with an electron density scaling factor $x_{ne} = 0.2$ (as in Biver et al. 2016). For the November 2015 observation with Odin, we assumed isotropic outgassing at 0.70 km s⁻¹ and T = 20 K: since the south pole of the nucleus was no longer oriented towards Earth three months after perihelion, and as the bulk of the outgassing was still expected to come from a direction close to that pole (Biver et al. 2019), there was no obvious reason to assume strong asymmetry with respect to the Earth direction in November 2015. It is important to note that SO is assumed to be produced by the photo-dissociation of SO_2 with a Haser parent scale length L_p equal to the SO₂ dissociation length $L_d(SO_2) = 4500$ km.

4.1. Relative abundances

Abundances relative to water, which were computed using $Q_{\rm H_2O} = 1.2 \times 10^{28} \, {\rm molec \, s^{-1}} \, (Q_{\rm H_2O} = 0.8 \times 10^{28} \, {\rm molec \, s^{-1}}$ in 2015), are provided in Table 4, compared to those obtained in situ by Rosetta/ROSINA and the range observed in comets.

Table 3. Production rates in 67P in November-December 2021.

$ \begin{array}{c ccccccccccccccccccccccccccccccccccc$	T. III.) / 1 1		D 1	T: (a)				
$\begin{array}{c ccccccccccccccccccccccccccccccccccc$		Molecule			Lines (a)				
$\begin{array}{c ccccccccccccccccccccccccccccccccccc$				(X10 molecs)					
$\begin{array}{c ccccccccccccccccccccccccccccccccccc$									
$\begin{array}{c ccccccccccccccccccccccccccccccccccc$									
$ \begin{array}{c ccccccccccccccccccccccccccccccccccc$									
$\begin{array}{c ccccccccccccccccccccccccccccccccccc$					_				
$\begin{array}{c ccccccccccccccccccccccccccccccccccc$									
$\begin{array}{c ccccccccccccccccccccccccccccccccccc$									
$\begin{array}{c ccccccccccccccccccccccccccccccccccc$	12/13.36	HCN	1.315	1.02 ± 0.11	1				
$\begin{array}{c ccccccccccccccccccccccccccccccccccc$	11/17.00	H_2O	1.225	1190 ± 440	1				
$\begin{array}{c ccccccccccccccccccccccccccccccccccc$	11/12.30	CH ₃ OH	1.217	11.1 ± 2.7	(6)				
$\begin{array}{c ccccccccccccccccccccccccccccccccccc$	11/13.20	CH_3OH	1.218	14.5 ± 3.2					
$ \begin{array}{c ccccccccccccccccccccccccccccccccccc$	11/14.15	CH_3OH	1.220	36.7 ± 6.6	(10)				
$\begin{array}{c ccccccccccccccccccccccccccccccccccc$	11/15.30		1.222	11.4 ± 1.4	(14)				
$\begin{array}{c ccccccccccccccccccccccccccccccccccc$	11/16.20	CH_3OH	1.223	17.4 ± 1.4	(17)				
$ \begin{array}{c ccccccccccccccccccccccccccccccccccc$	11/12.30	CS	1.217	0.42 ± 0.22	1				
$ \begin{array}{c ccccccccccccccccccccccccccccccccccc$	11/13.26	CS	1.218	0.74 ± 0.15	1				
$ \begin{array}{c ccccccccccccccccccccccccccccccccccc$	11/15.25	CS	1.222	0.64 ± 0.12	2				
$\begin{array}{c ccccccccccccccccccccccccccccccccccc$		CS	1.223	0.65 ± 0.12	2				
$\begin{array}{c ccccccccccccccccccccccccccccccccccc$		12–16 No	vember	2021 average					
$\begin{array}{c ccccccccccccccccccccccccccccccccccc$	11/12.0–16.2	HCN	1.221	1.10 ± 0.04	2				
$\begin{array}{c ccccccccccccccccccccccccccccccccccc$	11/12.3-16.3	CH_3CN	1.222	0.200 ± 0.038	(8)				
$\begin{array}{c ccccccccccccccccccccccccccccccccccc$	11/12.2-16.4	HNCO	1.221	0.54 ± 0.15					
$\begin{array}{c ccccccccccccccccccccccccccccccccccc$	11/12.2-16.2	CS	1.221	0.64 ± 0.07	2				
$\begin{array}{c ccccccccccccccccccccccccccccccccccc$		CS_d		$1.05 \pm 0.11^{(b)}$					
$\begin{array}{c ccccccccccccccccccccccccccccccccccc$	11/13.1-16.3		1.221	1.93 ± 0.35	1				
$\begin{array}{c ccccccccccccccccccccccccccccccccccc$	11/12.0-16.4		1.221	14.4 ± 0.7	18				
$\begin{array}{c ccccccccccccccccccccccccccccccccccc$	11/13.1-16.4		1.222		4				
$\begin{array}{c ccccccccccccccccccccccccccccccccccc$		_		$2.93 \pm 0.56^{(c)}$	4				
$\begin{array}{c ccccccccccccccccccccccccccccccccccc$	11/12.0–16.2	HNC	1.221	< 0.075	(1)				
$ \begin{array}{c ccccccccccccccccccccccccccccccccccc$									
$ \begin{array}{c ccccccccccccccccccccccccccccccccccc$	11/12.1-16.6		1.221						
$ \begin{array}{c ccccccccccccccccccccccccccccccccccc$	11/12.1-16.3		1.221	< 0.39					
$\begin{array}{c ccccccccccccccccccccccccccccccccccc$		_	1.222						
$\begin{array}{c ccccccccccccccccccccccccccccccccccc$		CO	1.222						
$ \begin{array}{c ccccccccccccccccccccccccccccccccccc$	11/12.2-16.4	SO_{nuc}	1.222	< 0.86					
$ \begin{array}{c ccccccccccccccccccccccccccccccccccc$		~ ~							
$ \begin{array}{c ccccccccccccccccccccccccccccccccccc$	11/12.0-16.4		1.222						
$ \begin{array}{c ccccccccccccccccccccccccccccccccccc$									
$\frac{11/12.0-16.4 \text{ CH}_3\text{CHO} 1.222}{12-13 \text{ December } 2021 \text{ average}}$ $\frac{12/12.3-13.4 \text{HCN} 1.313 1.1 \pm 0.1 1}{1}$									
$12/12.3-13.4$ HCN 1.313 1.1 ± 0.1 1									
	12–13 December 2021 average								
	12/12.3–13.4	HCN	1.313	1.1 ± 0.1	1				

Notes. ^(a)Number of lines used for the determination of Q, which are in parentheses when individual lines are not clearly detected. ^(b)CS_d: assuming that CS comes from a more distributed source than the usually assumed photo-dissociation of CS₂, using a parent scale length of 3000 km instead of 650 km (Roth et al. 2021; Biver et al. 2022). ^(c)H₂CO_d: we assume that H₂CO is produced in the coma with a Haser parent-scale length of 8000 km. ^(d)HNC_d: we assume that HNC is produced in the coma with a Haser parent-scale length of 1000 km (Cordiner et al. 2017). ^(e)Assuming a parent-scale length of 4500 km (L_d (SO₂)) for the case where SO is a daughter (SO_d) species and not coming from the nucleus (SO_{nuc}).

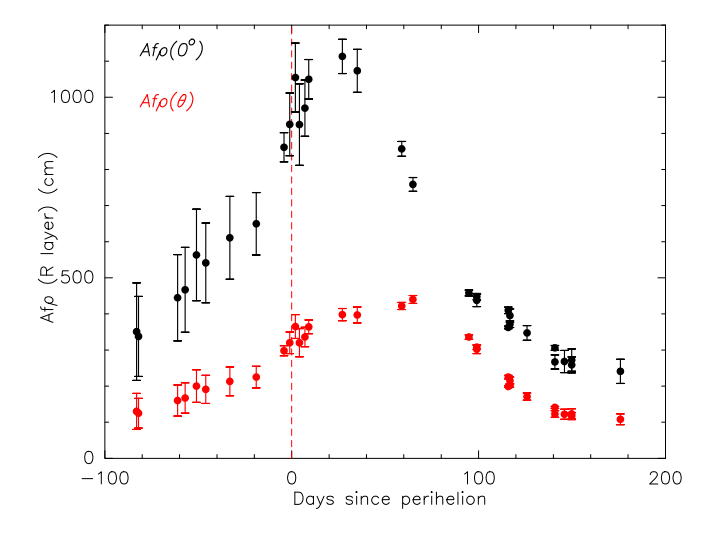


Fig. 10. Estimated values of $Af\rho$ and $Af\rho(0^{\circ})$ corrected for phase angle according to the formula proposed by Schleicher (2007). Measurements were carried out on images obtained with the red layer of the Bayer matrix of a Sony α 7s digital camera at the focus of a 40.7-cm diameter telescope ©N. Biver.

4.2. Upper limits

The various tunings cover most of the 1.3 mm receiver band $(60\,\mathrm{GHz})$ and a fraction of the 2 mm $(16\,\mathrm{GHz})$ and 3 mm $(8\,\mathrm{GHz})$ receiver bands. This is sufficient to cover most of the molecules and lines of interest. However, due to the moderate activity of the comet, significant upper limits on the abundance of only a select number of species have been measured and no significant isotopic ratios could be measured (the 3- σ sensitivity was never better than 7% of the main isotopologue). The limits on the abundance of non-detected cometary molecules is only of interest for a few molecules for which the 3- σ upper limits are comparable to that measured in other comets. These molecules, listed in Tables A.4 and 4, are HNC, HC₃N, CO, NH₂CHO, CH₃CHO, SO, SO₂, OCS, H₂CS, and HCOOH.

4.3. Evolution of the production rates

In 2021, the values of Q_{HCN} seem to show a plateau during this 10-40 days post-perihelion phase of peak activity, when the $Af\rho(0^{\circ})$ also seem to stall around 1100 cm (Fig. 10). Meanwhile, some daily fluctuations are seen, possibly related to the rotation of the nucleus (although the period is close to exactly half a day). Except for 14 November, the CH₃OH/HCN production rate ratio remained around 14 ± 3 and other species (CS, CH₃CN, and H₂S) do not show a significant variation in relative abundances. The CH₃OH production rate appeared 2.5× larger on 14 November, especially compared to HCN. The H₂CO production might also have been enhanced on that day. But in both cases, the S/N is also limited (CH₃OH production is only based on individual marginal lines, and not on the 166 or 242 GHz series), such that this result needs to be taken with caution. In December, the CH₃OH abundance is also higher (CH₃OH/HCN = 24 ± 9), but the detection is very marginal. Nevertheless, MIRO observed an increase in the methanol abundance after perihelion, which we see in the present observations and from the marginal detection in 2015, both yielding CH₃OH/H₂O ~ 2%, 5 weeks after perihelion.

Table 4. Molecular abundances.

Molecule	Name	Abundance relative to water in %						
		67P in 2021	67P in 2015 ^(a)	Rosetta (b)	in comets			
HCN	Hydrogen cyanide	0.09 ± 0.01	0.11 ± 0.02	0.2	0.08 - 0.25			
HNC	Hydrogen isocyanide	< 0.006	_	_	0.0015-0.035			
HNC_d	"	$< 0.009^{(c)}$	_	-				
CH ₃ CN	Methyl cyanide	0.017 ± 0.003	< 0.30	0.0059	0.008 - 0.054			
HC_3N	Cyanoacetylene	< 0.019	_	0.0004	0.002 - 0.068			
HNCO	Isocyanic acid	0.045 ± 0.013	_	0.027	0.009 - 0.080			
NH ₂ CHO	Formamide	< 0.033	_	0.004	0.016-0.022			
CO	Carbon monoxide	<4.6	_	0.3–3	0.4–35			
H_2CO	Formaldehyde	0.06 ± 0.01	< 0.8	0.5				
H_2CO_d	"	0.28 ± 0.05 ^(d)	$<1.5^{(d)}$	0.5	0.13- 1.4 ^(d)			
CH_3OH	Methanol	1.2 ± 0.1	2.1 ± 0.6	0.5 - 1.5	0.7 - 6.1			
HCOOH	Formic acid	< 0.21	_	0.013	0.03 - 0.18			
CH ₃ CHO	Acetaldehyde	< 0.14	_	0.047	0.05 - 0.08			
$\overline{H_2S}$	Hydrogen sulphide	0.16 ± 0.03	< 2.0	2.0	0.09-1.5			
CS	Carbon monosulphide	0.05 ± 0.01	< 0.25	$0.02^{(e)}$	0.05 - 0.20			
OCS	Carbonyl sulphide	< 0.54	_	0.07	0.05 - 0.40			
SO_d	Sulphur monoxide	$< 0.22^{(f)}$	_	0.071	$0.04 – 0.30^{(f)}$			
SO_2	Sulphur dioxide	< 0.23	_	0.127	0.03 - 0.23			
H_2CS	Thioformaldehyde	< 0.1	_	0.0027	0.009 – 0.090			

Notes. ^(a)Based on IRAM data with $Q_{\rm H_2O} = 8 \times 10^{27}$ molec s⁻¹ (Biver et al. 2019). ^(b)Based on Biver et al. (2019), Rubin et al. (2019), and Läuter et al. (2020). ^(c)Assuming a daughter distribution with $L_{\rm p} = 1.2$ –2.0 × $L_{\rm d}$ (H₂CO). ^(e)From CS₂ with ROSINA. ^(f)Assuming a daughter distribution with $L_{\rm p} = L_{\rm d}$ (SO₂).

5. Discussion and conclusion

The abundances and upper limits obtained in 2021 with IRAM 30-m are in full agreement with the 2015 IRAM 30-m results. The abundances relative to water found in 2021, complemented by those measured in situ with MIRO for NH3 and CO in 2015, are plotted against the findings of the ROSINA mass spectrometer in 2015 (Rubin et al. 2019; Läuter et al. 2020) in Fig. 11. We primarily selected the Läuter et al. (2020) results that are based on the long-term monitoring of the outgassing of 14 molecules and provide abundance ratios representative of the bulk abundances of the comet. The Rubin et al. (2019) paper gives abundances of a larger number of molecules, likely not as representative of the bulk composition, but at a time not too far from the peak of activity. Significant differences (data points departing from the diagonal line corresponding to equal abundances in the two datasets) are seen in Fig. 11 as compared with the ROSINA results.

5.1. Comparison with Rosetta in situ measurements

Since the 2021 observations were obtained one perihelion after the one that was followed by Rosetta (2014–2016), secular variations cannot be excluded. However, the outgassing pattern and the peak activity seemed very similar (Sect. 3). Discrepancies are more likely due to the different observing techniques.

The mass spectrometry (Rosetta/ROSINA in 2015–2016) relies on fragmentation patterns and ionisation efficiencies in the instrument, and on the modelling of the outgassing pattern of the nucleus to convert local density measurements into global

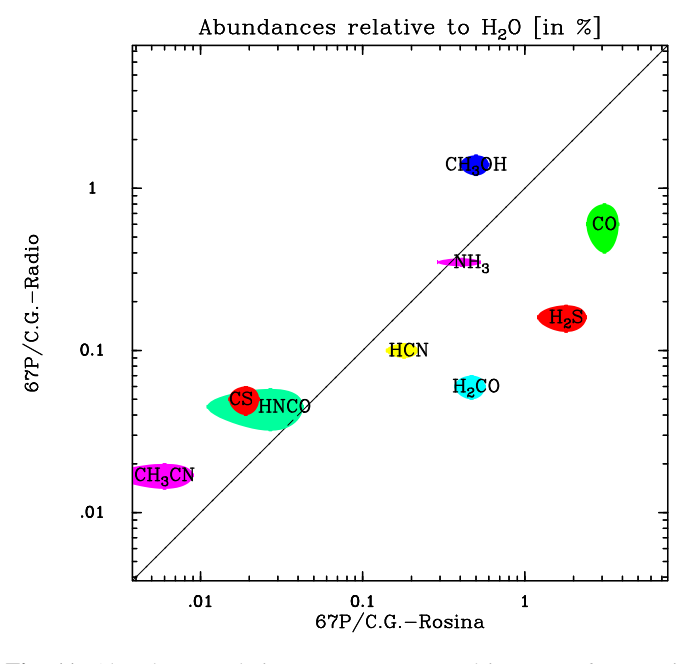


Fig. 11. Abundances relative to water measured in comet 67P. Vertical scale: Values obtained in the radio with IRAM 30-m observations in 2021, or with MIRO in 2015 for NH₃ and CO (well lower than the 2021 upper limit). Horizontal scale: Mean values measured in situ around 2015 perihelion with the Rosetta/ROSINA mass spectrometer, from Rubin et al. (2019) and Läuter et al. (2020). If the water production rate used for radio observations has to be re-evaluated to higher values, then all the points have to be shifted down. Each elliptical (in log scale) symbol covers the $\pm 1\sigma$ uncertainty domain.

production rates. The total local density was itself determined by a separate instrument (ROSINA-COPS), which measured a pressure depending on gas composition and velocity (Läuter et al. 2020). At the peak of activity in 2015, Rosetta never flew through the region of peak activity for safety reasons and mostly stayed over the terminator.

The radio spectroscopy, both in situ with MIRO or from remote observations, did sample the full coma (and measured the outgassing pattern), but it relies on a few rotational transitions that do not sample the full range of energy levels, and it is subject to biases due to excitation models. For strong lines (H₂O and H₂¹⁸O in situ) opacity effects are important and this increases uncertainties on the modelled line intensities. IRAM observations, with their 3000–13000 km beam size, get a more complete picture of the total outgassing, but they are more biased towards the mid to outer coma.

The comparison of the abundances of individual molecules provides important information:

CH₃OH. Over ten lines were detected at IRAM 30-m, spanning upper energy levels of 20-90 K, while the three lines observed with MIRO-sampled energies are from 40 to 186 K. Since the measured gas temperatures are within those ranges, we do not expect any noticeable bias. Generally, comparison of CH₃OH abundances derived from radio and infrared remote observations of comets agree, with some dispersion but no systematic biases. Regarding comet 67P, MIRO measured $Q_{\text{CH}_2\text{OH}} = 1.1 \pm 0.1 \times 10^{26} \text{ molec s}^{-1} \text{ (and } Q_{\text{H}_2\text{O}} = 0.8 \pm 0.1 \times 10^{26} \text{ molec s}^{-1} \text{ (and } Q_{\text{H}_2\text{O}} = 0.8 \pm 0.1 \times 10^{26} \text{ molec s}^{-1} \text{ (and } Q_{\text{H}_2\text{O}} = 0.8 \pm 0.1 \times 10^{26} \text{ molec s}^{-1} \text{ (and } Q_{\text{H}_2\text{O}} = 0.8 \pm 0.1 \times 10^{26} \text{ molec s}^{-1} \text{ (and } Q_{\text{H}_2\text{O}} = 0.8 \pm 0.1 \times 10^{26} \text{ molec s}^{-1} \text{ (and } Q_{\text{H}_2\text{O}} = 0.8 \pm 0.1 \times 10^{26} \text{ molec s}^{-1} \text{ (and } Q_{\text{H}_2\text{O}} = 0.8 \pm 0.1 \times 10^{26} \text{ molec s}^{-1} \text{ (and } Q_{\text{H}_2\text{O}} = 0.8 \pm 0.1 \times 10^{26} \text{ molec s}^{-1} \text{ (and } Q_{\text{H}_2\text{O}} = 0.8 \pm 0.1 \times 10^{26} \text{ molec s}^{-1} \text{ (and } Q_{\text{H}_2\text{O}} = 0.8 \pm 0.1 \times 10^{26} \text{ molec s}^{-1} \text{ (and } Q_{\text{H}_2\text{O}} = 0.8 \pm 0.1 \times 10^{26} \text{ molec s}^{-1} \text{ (and } Q_{\text{H}_2\text{O}} = 0.8 \pm 0.1 \times 10^{26} \text{ molec s}^{-1} \text{ (and } Q_{\text{H}_2\text{O}} = 0.8 \pm 0.1 \times 10^{26} \text{ molec s}^{-1} \text{ (and } Q_{\text{H}_2\text{O}} = 0.8 \pm 0.1 \times 10^{26} \text{ molec s}^{-1} \text{ (and } Q_{\text{H}_2\text{O}} = 0.8 \pm 0.1 \times 10^{26} \text{ molec s}^{-1} \text{ (and } Q_{\text{H}_2\text{O}} = 0.8 \pm 0.1 \times 10^{26} \text{ molec s}^{-1} \text{ (and } Q_{\text{H}_2\text{O}} = 0.8 \pm 0.1 \times 10^{26} \text{ molec s}^{-1} \text{ (and } Q_{\text{H}_2\text{O}} = 0.8 \pm 0.1 \times 10^{26} \text{ molec s}^{-1} \text{ (and } Q_{\text{H}_2\text{O}} = 0.8 \pm 0.1 \times 10^{26} \text{ molec s}^{-1} \text{ (and } Q_{\text{H}_2\text{O}} = 0.8 \pm 0.1 \times 10^{26} \text{ molec s}^{-1} \text{ (and } Q_{\text{H}_2\text{O}} = 0.8 \pm 0.1 \times 10^{26} \text{ molec s}^{-1} \text{ (and } Q_{\text{H}_2\text{O}} = 0.8 \pm 0.1 \times 10^{26} \text{ molec s}^{-1} \text{ (and } Q_{\text{H}_2\text{O}} = 0.8 \pm 0.1 \times 10^{26} \text{ molec s}^{-1} \text{ (and } Q_{\text{H}_2\text{O}} = 0.8 \pm 0.1 \times 10^{26} \text{ molec s}^{-1} \text{ (and } Q_{\text{H}_2\text{O}} = 0.8 \pm 0.1 \times 10^{26} \text{ molec s}^{-1} \text{ (and } Q_{\text{H}_2\text{O}} = 0.8 \pm 0.1 \times 10^{26} \text{ molec s}^{-1} \text{ (and } Q_{\text{H}_2\text{O}} = 0.8 \pm 0.1 \times 10^{26} \text{ molec s}^{-1} \text{ (and } Q_{\text{H}_2\text{O}} = 0.8 \pm 0.1 \times 10^{26} \text{ molec s}^{-1} \text{ (and } Q_{\text{H}_2\text{O}} = 0.8 \pm 0.1 \times 10^{26} \text{ molec s}^{-1} \text{ (and } Q_{\text{H}_2\text{O}} = 0.8 \pm 0.1 \times 10^{26} \text{ molec s}^{-1} \text{ (and } Q_{\text{H}_2\text{O}} = 0.8 \pm 0.1 \times 10^{26} \text{ molec s}^{-1} \text{ ($ 10²⁸ molec s⁻¹, Biver et al. 2019) two weeks after perihelion as compared to $1.4 \pm 0.1 \times 10^{26}$ molec s⁻¹ (with $Q_{H_2O} = 1.2 \pm 0.3 \times 10^{26}$ 10²⁸ molec s⁻¹) in 2021 at the same orbital phase, corresponding to a similar methanol abundance ($\sim 1.3\%$). The difference in absolute production rate can be attributed either to a closer perihelion in 2021 (1.211 vs 1.244 au) increasing the outgassing rates or some minor production from a distributed source (icy grains) in the coma. Rosetta/ROSINA derived a maximum Q_{CH_2OH} of $1.14 \pm 0.05 \times 10^{26}$ molec s⁻¹ (Läuter et al. 2020) very similar to the Rosetta/MIRO value; however, due to a water peak production rate twice as high, they inferred a lower abundance relative to water.

CS and H_2S . Assuming that CS is created by the photodissociation of CS_2 yields an overabundance of CS by a factor of three as compared to the Rosetta/ROSINA abundance of CS_2 . But it has been shown that CS is produced from a distributed source more extended than the photo-dissociation scale length of CS_2 (Roth et al. 2021; Biver et al. 2022, see for example). This might explain the lower CS_2 production rate measured by Rosetta/ROSINA.

We note that H₂S was found to be under-abundant in comet 67P based on IRAM observations (Table 4). The trend is observed on all three days when H₂S was detected (Table A.4). Other JFCs, such as 21P/Giacobini-Zinner (Biver et al. 2021a) or 73P/Schwassmann-Wachmann 3, also showed low abundances of H₂S. But the Rosetta/ROSINA value on the other hand suggests a rather high production and abundance (2%) of H₂S relative to water. This value is even higher than the largest abundance observed in other comets. The discrepancy between the 2015 ROSINA result and the 2021 IRAM 30-m measurement is larger than a factor of ten. Even the peak H₂S production rate from Läuter et al. (2020), 4.4×10^{26} molec s⁻¹, is higher than the upper limit found with IRAM 2015 observations $(Q_{\rm H_2S} < 1.6 \times 10^{26} \, \rm molec \, s^{-1}, \, Table \, 2)$. It is very difficult to find realistic excitation conditions to increase the production rate retrieved from radio observations by a factor larger than ten: for

example, we would need to increase, at the same time, (i) the gas temperature ($T \sim 300 \text{K}$) by a factor of eight, (ii) the collisional cross section ($\sigma_c > 2 \times 10^{-13} \, \text{cm}^2$) by a factor of ten, and (iii) the photo-dissociation rate ($\beta_0 \sim 1.5 \times 10^{-3} \, \text{s}^{-1}$) by a factor of six. Adjusting only one of the parameters within realistic values is not sufficient. But with such parameters, the abundances of H₂S in some other comets would increase to unrealistic values (>7%), or they would be incompatible with the detection of other H₂S lines. So the high abundance derived with ROSINA also needs to be checked for potential biases.

 H_2CO . Formaldehyde is detected with a S/N of 3–4 for the two strongest lines. If we assume that it comes from the nucleus, the radio observation yields a production rate of H_2CO $20\times$ lower than for CH_3OH , while Läuter et al. (2020) with Rosetta/ROSINA found a similar production rate around perihelion. But radio observations of other comets have shown that, for the majority, most of H_2CO comes from a distributed source, with a typical scale length that would scale to around 8000 km for comet 67P (e.g. Biver et al. 2022). In that case, the abundance of the parent of H_2CO is four times larger, making it closer to that of methanol as found by ROSINA; however, at the distance sampled by Rosetta, most of the formaldehyde should have still been in its parent form. This raises a question as to whether the unknown parent of formaldehyde in comet 67P could have been degraded into H_2CO inside the ROSINA instrument.

Those discrepancies, between the abundances of H_2S and H_2CO measured remotely in the radio in 2021 and in situ in 2015 via mass spectrometry, highlight the issue of having strong biases due to the different techniques and models used to interpret the observed quantities.

5.2. Comparison with other comets

Based on the results obtained with the IRAM 30-m telescope, comet 67P displays abundances typical of comets that are not enriched in highly volatiles species, sharing similarities with 21P/Giacobini-Zinner, for example (Biver et al. 2021b), another carbon-chain depleted comet from the taxonomy of A'Hearn et al. (1995). Abundances of HNC, HC₃N, CO, SO, and SO₂ larger than our upper limits in comet 67P have been measured in some comets (Table 4 and Biver & Bockelée-Morvan 2019, and especially in comet Hale-Bopp); however, except for HNC which is only identifiable via its rotational lines, in situ observations of 2015 with ROSINA suggest abundances below our upper limits in comet 67P.

5.3. Conclusion

We have detected rotational lines of eight molecular species (H₂O, HCN, CH₃OH, H₂S, CS, CH₃CN, H₂CO, and HNCO) in the coma of comet 67P/Churyumov-Gerasimenko at its very favourable perihelion in November 2021.

- From the line profiles, all species seem to come from a collimated jet from the sub-solar to south-pole region, containing ~80% of the gas ejected at a speed of 0.86 km s⁻¹. This outgassing pattern is the same as observed in situ in 2015.
- We derived a gas temperature T = 36 K (with a ~3000 km beam), also similar to that measured in the coma by MIRO in 2015 at large distances from the nucleus ($\gg 100$ km).
- The production rate profile, as well as the dust production tracer $Af\rho(0)$, suggest that production peaked during our observation period, 10–40 days after perihelion.
- We measured the abundances relative to water for seven species: HCN, CH₃OH, H₂S, CS, CH₃CN, H₂CO, and HNCO. We also obtained significant upper limits on the

- abundances of HNC, CO, HC₃N, SO, and SO₂; although, they were not lower than the abundances observed by Rosetta/ROSINA. These abundances fall in the range of those measured in other comets, especially the volatile poor and carbon-chain depleted ones.
- One of the main objectives of this investigation was to compare remote and in situ measurement of the composition of the coma. The comparison has revealed some strong discrepancies, assuming that the comet composition did not change between 2015 and 2021, as suggested by its overall activity behaviour, and HCN and CH₃OH production rates. The two major issues are the abundance of H₂S, which is an order of magnitude lower than measured by Rosetta/ROSINA, and that of the H₂CO coming from the nucleus, which is also found to be much less abundant (H₂CO/CH₃OH 20× lower than found by ROSINA). This later discrepancy could be explain if the parent responsible for the distributed source of H₂CO observed in the radio, was degraded into H₂CO when measured by ROSINA (as for example a weakly bond dimer).

There is no easy explanation for a bias in the estimate of a $\rm H_2 S$ or $\rm H_2 CO$ abundance derived from radio observations. However, the larger discrepancy with in situ mass spectrometry needs to be solved in order to validate both the large sample of remote measurements of comet compositions and in situ measurements.

Acknowledgements. This work is based on observations carried out under projects number 001-15, 001-21, 100-21 with the IRAM 30-m telescope. IRAM is supported by the Institut Nationnal des Sciences de l'Univers (INSU) of the French Centre national de la recherche scientifique (CNRS), the Max-Planck-Gesellschaft (MPG, Germany) and the Spanish IGN (Instituto Geográfico Nacional). We gratefully acknowledge the support from the IRAM staff for its support during the observations. The data were reduced and analysed thanks to the use of the GILDAS, class software (http://www.iram.fr/IRAMFR/ GILDAS). This research has been supported by the Programme National de Planétologie de l'Institut des Sciences de l'Univers (INSU). The Observatoire Radioastronomique de Nançay is operated by the Observatoire de Paris associated with the CNRS and with the University of Orléans. Part of this research was carried out at the Jet Propulsion Laboratory, California Institute of Technology, under a contract with the National Aeronautics and Space Administration (80NM0018D0004). B. P. Bonev and N. Dello Russo acknowledge support of NSF grant AST-2009398 and NASA grant 80NSSC17K0705, respectively. N. X. Roth acknowledges support by the NASA Postdoctoral Program at the NASA

Goddard Space Flight Center, administered by Universities Space Research Association under contract with NASA. M.A. Cordiner is supported in part by the National Science Foundation (under Grant No. AST-2009253). S.N. Milam, M.A. Cordiner, and N.X. Roth acknowledge the Planetary Science Division Internal Scientist Funding Program through the Fundamental Laboratory Research (FLaRe) work package, as well as the NASA Astrobiology Institute through the Goddard Center for Astrobiology (proposal 13-13NAI7-0032). M. DiSanti acknowledges support through NASA Grant 18-SSO18_2-0040.

A'Hearn, M. F., Millis, R. L., Schleicher, D. G., Osip, D. J., & Birch, P. V. 1995,

References

Icarus, 118, 223

375, 20160249

```
Accomazzo, A., Ferri, P., Lodiot, S., et al. 2016, Acta Astronaut., 126, 190
Accomazzo, A., Ferri, P., Lodiot, S., et al. 2017, Acta Astronaut., 136, 354
Biver, N., & Bockelée-Morvan, D. 2019, ACS Earth Space Chem., 3, 1550
Biver, N., Bockelée-Morvan, D., Crovisier, J., et al. 2002, Earth Moon Planets,
   90, 323
Biver, N., Moreno, R., Bockelée-Morvan, D., et al. 2016, A&A, 589, A78
Biver, N., Bockelée-Morvan, D., Hofstadter, M., et al. 2019, A&A, 630, A19
Biver, N., Bockelée-Morvan, D., Boissier, J., et al. 2021a, A&A, 648, A49
Biver, N., Bockelée-Morvan, D., Lis, D.C., et al. 2021b, A&A, 651, A25
Biver, N., Boissier, J., Bockelée-Morvan, D., et al. 2022, A&A, 668, A171
Bockelée-Morvan, D., Crovisier J., Colom P., & Despois D. 1994, A&A, 287,
Bockelée-Morvan, D., Calmonte, U., Charnley, S., et al. 2015, Space Sci. Rev.,
   197, 47
Bonev, B., Dello Russo, N., Kawakita, H., et al. 2022, BAAS, 54,
   e-id 2022n8i411p05
Carter, M., Lazareff, R., Maier, D., et al. 2012, A&A, 538, A89
Cordiner, M.A., Remijan, A.J., Boissier, J., et al. 2014, ApJ, 792, L2
Cordiner, M.A., Boissier, J., Charnley, S.B., et al. 2017, ApJ, 838, 147
Crovisier, J., Colom, P., Gérard, E., Bockelée-Morvan, D., & Bourgois, G. 2002,
   A&A, 393, 1053
Despois, D., Gerard, E., Crovisier, J., & Kazes, I. 1981, A&A, 99, 320
Frisk, U., Hagström, M., Ala-Laurinaho, J., et al. 2003, A&A, 402, L27
Gibb, E., Roth, N., Khan, Y., et al. 2022, BAAS, 54, e-id 2022n8i411p01
Läuter, M., Kramer, T., Rubin, M., & Altwegg, K. 2020, MNRAS, 498, 3995
Müller, H. S. P., Schlöder, F., Stutzki J., & Winnewisser, G. 2005, J. Mol. Struct.,
Pickett, H. M., Poynter, R. L., Cohen, E. A., et al. 1998, J. Quant. Spec. Radiat.
   Transf., 60, 883
Roth, N.X., Milam, S.N., Cordiner, M.A., et al., 2021, ApJ, 921, 14
Rubin, M., Altwegg, K., Balsiger, H., et al. 2019, MNRAS, 489, 594
Schleicher, D.G., 2007, Icarus, 191, 322
Schleicher D. G., & A'Hearn M. F. 1988, ApJ, 331, 1058
```

Snodgrass, C., A'Hearn, M. F., Aceituno, F., et al. 2017, Phil. Trans. R. Soc. A,

Appendix A: Tables

Table A.1. Log of observations in 2015.

UT date	< r _h >	< Δ >	Phase ^(a)	Tel.	Integ. time	$pwv^{(b)}$	Mode ^(d)	Freq. range
(mm/dd.d-dd.d)	(au)	(au)			$(\min)^{(c)}$	(mm)		(GHz)
09/18.25-18.34	1.320	1.786	33.7°	IRAM	87	3.8	WSW	248.0-255.7, 263.6-271.4
18.35-18.36	1.320	1.786	33.7°	IRAM	23	3.8	FSW	248.0-255.7, 263.6-271.4
18.36-18.40	1.320	1.786	33.7°	IRAM	37	3.8	WSW	248.0-255.7, 263.6-271.4
18.41-18.57	1.321	1.786	33.7°	IRAM	159	6-13	FSW	223.8-231.6, 239.5-247.3
09/19.23-19.35	1.324	1.787	33.7°	IRAM	121	5.9	WSW	248.0-255.7, 263.6-271.4
19.37-19.58	1.325	1.787	33.7°	IRAM	205	6.5	WSW	223.8-231.6, 239.5-247.3
09/20.23-20.40	1.328	1.788	33.7°	IRAM	154	3-5	WSW	248.0-255.7, 263.6-271.4
20.41-20.55	1.329	1.788	33.7°	IRAM	135	7-10	WSW	223.8-231.6, 239.5-247.3
09/21.24-21.35	1.333	1.789	33.7°	IRAM	47	14-10	WSW	83.2-90.9, 139.6-147.4
09/22.24-22.36	1.337	1.790	33.6°	IRAM	117	3.8	WSW	163.0-170.8, 301.8-309.6
11/09.47–12.10	1.64	1.79	33.2°	Odin	1960	0.0	DSW	556.4–557.4

Notes. ^(a)Phase angle. ^(b)Mean precipitable water vapour in the atmosphere above the telescope.

Color Total (offset positions included) integration time (ON+OFF) on the source. (d) Observing mode: WSW = Wobbler SWitching (reference at $\pm 3'$); FSW = Frequency SWitching ($\pm 7.4 - 7.8$ MHz); DSW = Dicke SWitching (reference at $\sim 40^{\circ}$).

Table A.2. Log of observations in 2021.

							- ()	
UT date	$< r_h >$	$<\Delta>$	Phase ^(a)	Tel.	Integ. time	$pwv^{(b)}$	$Mode^{(d)}$	Freq. range
(mm/dd.d-dd.d)	(au)	(au)			$(\min)^{(c)}$	(mm)		(GHz)
11/12.01–12.17	1.217	0.418	48.4°	IRAM	164	4.2	WSW	248.7-256.5, 264.4-272.2
12.24-12.37	1.217	0.418	48.3°	IRAM	121	5.1	WSW	240.4-248.1, 256.0-263.8
11/13.01-13.08	1.218	0.418	48.2°	IRAM	69	5.5	WSW	248.7-256.5, 264.4-272.2
13.11-13.18	1.219	0.418	48.1°	IRAM	79	6.4	WSW	146.9-154.7, 162.6-170.4
13.23-13.40	1.219	0.418	48.1°	IRAM	159	6.5	WSW	146.9-154.7, 162.6-170.4
11/13.98-14.04	1.220	0.418	47.9°	IRAM	65	4.4	WSW	83.2-90.9, 225.0-232.8
14.07-14.08	1.220	0.418	47.9°	IRAM	14	4.2	WSW	248.7-256.5, 264.4-272.2
14.10-14.15	1.220	0.418	47.9°	IRAM	44	4.0	PSW	248.7-256.5, 264.4-272.2
14.25-14.37	1.220	0.418	47.8°	IRAM	99	6-5	PSW	209.7-217.5, 225.4-233.1
11/14.98-15.01	1.221	0.418	47.7°	IRAM	28	3.2	PSW	83.2-90.9, 225.0-232.8
15.04-15.10	1.222	0.418	47.6°	IRAM	60	4.1	PSW	248.7-256.5, 264.4-272.2
15.13-15.18	1.222	0.418	47.6°	IRAM	44	3.2	PSW	146.9-154.7, 162.6-170.4
15.23-15.28	1.222	0.418	47.6°	IRAM	48	2.5	PSW	146.9-154.7, 162.6-170.4
15.29-15.37	1.222	0.418	47.6°	IRAM	64	1.5	PSW	240.4-248.1, 256.0-263.8
11/15.99-16.06	1.223	0.419	47.4°	IRAM	64	1.4	PSW	224.9-232.7, 240.6-248.3
16.08-16.15	1.223	0.419	47.4°	IRAM	62	1.2	PSW	248.7-256.5, 264.4-272.2
16.22-16.30	1.224	0.419	47.3°	IRAM	76	2.0	PSW	146.9-154.7, 162.6-170.4
16.32-16.38	1.224	0.419	47.3°	IRAM	64	1.2	PSW	217.8-225.6, 233.5-241.2
12/12.35–12.36	1.311	0.438	35.1°	IRAM	9	2.8	WSW	248.4-256.5, 264.4-272.5
12/13.35-13.37	1.315	0.440	34.4°	IRAM	19	0.7	WSW	248.4-256.5, 264.4-272.5
11/16.99–17.01	1.225	0.419	47.1°	Odin	2	0.0	DSW	556.4–557.4

Notes. (a) Phase angle. (b) Mean precipitable water vapour in the atmosphere above the telescope. (c) Total (offset positions included) integration time (ON+OFF) on the source. (d) Observing mode: WSW = Wobbler SWitching (reference at $\pm 3'$); PSW = Position SWitching (reference at 5'); DSW = Dicke SWitching (reference at $\sim 40^{\circ}$).

Table A.3. Line intensities from Odin and IRAM observations in 2015

Date ^(a)	Molecule	Transition	Frequency(b)	offset ^(c)	Intensity	Doppler shift
(yyyy/mm/dd.dd)			(MHz)	(")	$(K \text{ km s}^{-1})$	$(km s^{-1})$
2015/11/10.8	H ₂ O	$1_{10} - 1_{01}$	556935.988	10	< 0.057	
2015/09/19.3	HCN	3-2	265886.434	1.5	0.060 ± 0.012	-0.29 ± 0.13
2015/09/21.30	HCN	1-0	88631.848	0.9	< 0.066	
2015/09/21.30	CH_3CN	8-7	147174.588-147149.068	0.9	sum(4lines) < 0.123	
2015/09/22.30	CH_3CN	9-8	165569.082-165540.377	1.5	sum(4lines) < 0.051	
2015/09/19.3	CS	5-4	244935.557	2.3	< 0.043	
2015/09/21.30		3-2	146969.029	0.9	< 0.064	
2015/09/22.30	H_2S	$1_{10} - 1_{01}$	168762.762	1.5	< 0.029	
2015/09/21.30	CH_3OH	$3_{K}-2_{K}$	143865.801-146368.342	0.9	sum(7lines) < 0.153	
2015/09/22.30	CH_3OH	$J_1 - J_0 \mathrm{E}$	165050.175-165678.649	1.5	sum(6lines) < 0.069	
2015/09/19.3	CH_3OH	$5_K - 4_K$	241700.168-241904.401	2.3	$sum(4lines)=0.037 \pm 0.021$	
2015/09/19.4	CH_3OH	$5_2 - 4_{-1}E$	266838.123	1.5	< 0.033	
2015/09/22.30	CH_3OH	$1_1 - 1_0 A^{-+}$	303366.893	1.3	0.057 ± 0.030	-0.16 ± 0.32
		$2_1 - 2_0 A^{-+}$	304208.324		0.022 ± 0.026	-0.07 ± 0.37
		$3_1 - 3_0 A^{-+}$	305473.472		0.050 ± 0.031	-0.49 ± 0.51
		$4_1 - 4_0 A^{-+}$	307165.911		0.061 ± 0.035	-0.24 ± 0.36
		$5_1 - 5_0 A^{-+}$	309290.354		0.001 ± 0.039	
2015/09/21.30	H_2CO	$2_{12} - 1_{11}$	140839.518	0.9	< 0.060	
2015/09/19.3		$3_{12} - 2_{11}$	225697.772	2.3	< 0.033	
2015/09/19.3	CO	2-1	230538.000	2.1	< 0.041	

Notes. ^(a)Dates are rounded to the nearest tenth of a day for averages over several days. ^(b)From Müller et al. (2005) and Pickett et al. (1998). For HCN the strongest hyperfine components are in the integration window and the integrated intensity takes into account the weaker ones according to their statistical weight. ^(c)Average radial pointing offset.

Table A.4. Line intensities from Odin and IRAM observations.

Date ^(a)	Molecule	Transition	Frequency ^(b)	offset ^(c)	Intensity	Doppler shift
(yyyy/mm/dd.dd)			(MHz)	(")	$(K \text{ km s}^{-1})$	$(km s^{-1})$
2021/11/17.00	H ₂ O	$1_{10} - 1_{01}$	556935.988	38	1.276 ± 0.430	-0.10 ± 0.24
2021/11/12.09	HCN	3-2	265886.434	1.4	0.363 ± 0.026	-0.30 ± 0.04
				4.9	0.256 ± 0.050	-0.45 ± 0.14
				8.0	0.131 ± 0.091	-0.90 ± 0.95
2021/11/13.05	HCN	3-2	265886.434	1.3	0.407 ± 0.051	-0.38 ± 0.07
				5.1	0.269 ± 0.134	-0.02 ± 0.31
2021/11/14.11	HCN	3-2	265886.434	2.5	0.332 ± 0.034	-0.36 ± 0.07
				5.4	0.197 ± 0.063	-0.48 ± 0.22
				7.3	0.200 ± 0.153	$+0.01 \pm 0.28$
2021/11/15.07	HCN	3-2	265886.434	1.1	0.387 ± 0.033	-0.45 ± 0.06
				4.8	0.363 ± 0.069	-0.41 ± 0.11
				6.3	0.274 ± 0.121	-0.22 ± 0.26
2021/11/16.12	HCN	3-2	265886.434	1.2	0.489 ± 0.017	-0.31 ± 0.02
				4.9	0.297 ± 0.039	-0.29 ± 0.07
				7.5	0.277 ± 0.057	-0.33 ± 0.13
				9.7	0.104 ± 0.092	-1.03 ± 0.90
2021/12/12.35	HCN	3-2	265886.434	0.5	0.432 ± 0.098	-0.05 ± 0.13
2021/12/13.36	HCN	3-2	265886.434	0.6	0.393 ± 0.041	-0.15 ± 0.05
2021/11/14.3	HCN	1-0	88631.848	2.3	0.031 ± 0.012	-0.51 ± 0.32
2021/11/14.7	HNC	3-2	271981.142	1.4	< 0.036	
2021/11/14.7	CH_3CN	8,0-7,0	147174.588	1.5	0.008 ± 0.003	-0.43 ± 0.18
		8,1-7,1	147171.752		0.010 ± 0.003	
2021/11/14.9	CH_3CN	9,0-8,0	165569.082	1.4	0.009 ± 0.004	-0.18 ± 0.23
		9,1-8,1	165565.891		0.011 ± 0.004	
2021/11/16.35	CH ₃ CN	12,0-11,0	220747.261	1.0	0.019 ± 0.011	ı
		12,1-11,1	220743.011		0.007 ± 0.010	
2021/11/16.35	CH ₃ CN	13,0-12,0	239137.916	1.0	0.028 ± 0.013	-0.53 ± 0.27
	-	13,1-12,1	239133.313		0.029 ± 0.014	
2021/11/14.6	CH ₃ CN	14,0-13,0	257527.383	2.0	-0.002 ± 0.009	ı
	-	14,1-13,1	257522.427		0.011 ± 0.009	
2021/11/14.7	HNCO	$7_{07} - 6_{06}$	153865.086	1.5	0.009 ± 0.003	-0.53 ± 0.31

Table A.4. continued.

			40			
Date ^(a)	Molecule	Transition	Frequency(b)	offset ^(c)	Intensity	Doppler shift
(yyyy/mm/dd.dd)			(MHz)	(")	$(K \text{ km s}^{-1})$	$(km s^{-1})$
2021/11/16.35		$10_{010} - 9_{09}$	219798.274	1.0	0.009 ± 0.009	-0.50 ± 0.81
2021/11/15.0		$11_{011} - 10_{010}$	241774.032	1.7	0.007 ± 0.008	
2021/11/14.6		$12_{012} - 11_{011}$	263748.625	2.0	0.011 ± 0.013	-0.11 ± 0.67
2021/11/13.26	H_2S	$1_{10} - 1_{01}$	168762.762	1.6	0.035 ± 0.010	-0.28 ± 0.22
2021/11/15.21		$1_{10} - 1_{01}$	168762.762	1.2	0.029 ± 0.008	-0.10 ± 0.19
2021/11/16.26		$1_{10} - 1_{01}$	168762.762	1.5	0.020 ± 0.008	-0.72 ± 0.40
2021/11/15.0	CS	5-4	244935.557	1.7	0.041 ± 0.008	-0.56 ± 0.15
2021/11/14.7		3-2	146969.029	1.5	0.025 ± 0.003	-0.20 ± 0.09
2021/11/14.7	H_2CO	$2_{11} - 1_{10}$	150498.334	1.5	0.010 ± 0.003	-0.51 ± 0.27
2021/11/14.31	_	$3_{13} - 2_{12}$	211211.469	2.0	0.017 ± 0.016	$+0.79 \pm 0.97$
2021/11/16.35		$3_{03} - 2_{02}$	218222.191	1.0	0.014 ± 0.009	-0.10 ± 0.39
2021/11/15.3		$3_{12} - 2_{11}$	225697.772	2.0	0.025 ± 0.007	$+0.07 \pm 0.17$
2021/11/15.3	CO	2-1	230538.000	2.0	< 0.023	
2021/11/14.9	CH ₃ OH	$1_1 - 1_0 E$	165050.175	1.4	0.009 ± 0.004	$+0.12 \pm 0.25$
	- 3-	$2_1 - 2_0 E$	165061.130		0.014 ± 0.004	-0.09 ± 0.21
		$\frac{1}{3_1} - \frac{1}{3_0}$ E	165099.240		0.015 ± 0.004	-0.51 ± 0.19
		$4_1 - 4_0 E$	165190.475		0.021 ± 0.004	-0.45 ± 0.15
		$5_1 - 5_0 E$	165369.341		0.009 ± 0.004	-0.42 ± 0.28
		$6_1 - 6_0 E$	165678.649		0.013 ± 0.005	-0.18 ± 0.28
		$7_1 - 7_0 E$	166169.210		0.007 ± 0.004	-0.80 ± 0.66
	CH ₃ OH	$3_2 - 2_1 E$	170060.581		0.027 ± 0.006	$+0.02 \pm 0.15$
2021/11/14.31	CH ₃ OH	$1_1 - 0_0 E$	213427.118	2.0	0.025 ± 0.015	-0.59 ± 0.55
2021,11,1101	011,011	$5_1 - 4_2 E$	216945.559		0.034 ± 0.014	-0.13 ± 0.27
2021/11/16.35	CH ₃ OH	$4_2 - 3_1 E$	218440.050	1.0	0.024 ± 0.009	-0.30 ± 0.29
2021/11/15.3	CH ₃ OH	$8_{-1} - 7_0 E$	229758.811	2.0	0.017 ± 0.008	$+0.37 \pm 0.37$
2021, 11, 10.0	011,011	$3_{-2} - 4_{-1}E$	230027.002		0.016 ± 0.007	-0.47 ± 0.34
2021/11/16.35	CH ₃ OH	$5_1 - 4_1 A$	239746.220	1.0	0.028 ± 0.010	-0.32 ± 0.23
2021/11/15.0	CH ₃ OH	$5_0 - 4_0 E$	241700.168	1.7	0.058 ± 0.007	-0.44 ± 0.09
2021/11/10:0	0113011	$5_{-1} - 4_{-1}E$	241767.247	1.7	0.036 ± 0.008	-0.46 ± 0.17
		$5_0 - 4_0 \text{ A}$	241791.367		0.029 ± 0.007	-0.59 ± 0.23
		$5_3 - 4_3 \text{ A}$	241832.910		0.008 ± 0.007	-0.40 ± 0.63
		$5_2 - 4_2 A^-$	241842.287		0.012 ± 0.007	-0.58 ± 0.49
		$\frac{32}{5_3} - \frac{12}{4_3}$ E	241843.608		-0.001 ± 0.007	0.50 ± 0.17
		$5_{-3} - 4_{-3}E$	241852.299		0.004 ± 0.007 0.004 ± 0.007	
		$5_{1} - 4_{1}E$	241879.038		0.028 ± 0.007	-0.36 ± 0.18
		$5_2 - 4_2 A^+$	241887.678		0.020 ± 0.007 0.000 ± 0.007	0.50 ± 0.10
		$5_{\pm 2} - 4_{\pm 2}E$	241904.401		0.026 ± 0.007	-0.38 ± 0.24
		$5_{\pm 2}$ $4_{\pm 2}$ $1_{\pm 2}$ 1_{\pm	243915.811		0.020 ± 0.000 0.030 ± 0.007	-0.34 ± 0.17
2021/11/14.7	CH ₃ OH	$3_3 - 3_2 A^{+-}$	251917.057	1.4	0.030 ± 0.007 0.020 ± 0.010	-0.40 ± 0.35
2021/11/14./	C113O11	$3_3 - 3_2 A^{-+}$	251905.720	1.4	0.020 ± 0.010 0.011 ± 0.010	$+0.68 \pm 0.85$
		$4_3 - 4_2 A^{+-}$	251900.439		0.011 ± 0.010 0.013 ± 0.010	-0.52 ± 0.62
		$4_3 - 4_2 A^{-+}$	251866.510		0.013 ± 0.010 0.020 ± 0.011	$+0.34 \pm 0.42$
		$5_3 - 5_2 A^{+-}$	251890.868		0.020 ± 0.011 0.008 ± 0.011	10.34 ± 0.42
		$5_3 - 5_2 A^{-+}$	251811.936		0.000 ± 0.011 0.002 ± 0.010	
		$6_3 - 6_2 A^{+-}$	251895.703		0.002 ± 0.010 0.015 ± 0.011	-0.66 ± 0.68
		$6_3 - 6_2 A^{-+}$	251738.411		-0.007 ± 0.011 -0.007 ± 0.010	0.00 ± 0.00
		$7_3 - 7_2 A^{+-}$	251923.671		0.007 ± 0.010 0.009 ± 0.010	
		$7_3 - 7_2 A$ $7_3 - 7_2 A^{-+}$	251641.754		0.009 ± 0.010 0.013 ± 0.011	-0.86 ± 0.87
	CH ₃ OH	$7_3 - 7_2 R$ $5_2 - 4_{-1}E$	266838.123	1.4	0.013 ± 0.011 0.031 ± 0.008	-0.80 ± 0.87 -0.17 ± 0.15
2021/11/14.6	CH ₃ OH	$3_2 - 4_{-1}E$ $2_1 - 1_0E$	261805.736	2.0	0.031 ± 0.008 0.026 ± 0.009	-0.17 ± 0.13 -0.01 ± 0.19
2021/11/14.0	СПЗОП	∠ ₁ = 10E	201003.730	2.0	0.020 ± 0.009	-0.01 ± 0.19

Notes. ^(a)Dates are rounded to the nearest tenth of a day for averages over several days. ^(b)From Müller et al. (2005) and Pickett et al. (1998). For HCN the strongest hyperfine components are in the integration window and the integrated intensity takes into account the weaker ones according to their statistical weight. ^(c)Average radial pointing offset.